Triblock terpolymer directed self-assembly of mesoporous TiO_2 - high performance photoanodes for solid state dye-sensitized solar cells

Pablo Docampo, Morgan Stefik, Stefan Guldin, Robert Gunning, Nataliya Yufa, Ning Cai, Peng Wang, Ullrich Steiner, Ulrich Wiesner, and Henry J. Snaith

We present a new self-assembly platform for the fast and straightforward synthesis of bicontinuous, mesoporous TiO_2 films, based on the triblock terpolymer poly(isoprene-*b*-styrene-*b*-ethylene oxide). *This new material allows the co-assembly of the metal oxide as a fully interconnected minority phase which results in a highly porous photoanode with strong advantages over the state-of-the-art nanoparticle based photoanodes employed in solid-state dye-sensitized solar cells (DSC). Devices fabricated through this triblock terpolymer route exhibit a high availability of sub-bandgap states distributed in a narrow and low enough energy band, which maximizes photoinduced charge generation from a state-of-the-art organic dye, C220. As a consequence, the co-assembled mesoporous metal oxide system outperformed the conventional nanoparticle based electrodes fabricated and tested under the same conditions, exhibiting solar power conversion efficiencies of over 5%.*

1 Introduction

Dye-sensitized solar cells (DSCs) consist of three main device components: an electron conducting network which is sensitized by a light-absorbing dye and surrounded by an

P. Docampo, Dr. R. Gunning, Dr. H.J. Snaith
Department of Physics, Clarendon Laboratory, University of Oxford, Parks Road, Oxford OX1 3PU, UK
e-mail:h.snaith1@physics.ox.ac.uk

S. Guldin, Dr. N.A. Yufa, Prof. U. Steiner
Department of Physics, University of Cambridge,
J. J. Thomson Avenue, Cambridge CB3 0HE, UK

Dr. M. Stefik †, Prof. U. Wiesner
Department of Materials Science & Engineering, Cornell University,
Ithaca, New York 14853, USA
† Now at: Laboratory of Photonic and Interfaces, Institute of Physical Chemistry, École Polytechnique Fédérale de Lausanne, 1015 Lausanne, Switzerland

N. Cai, P. Wang
State Key Laboratory of Polymer Physics and Chemistry, Changchun Institute of Applied Chemistry, Chinese Academy of Sciences, Changchun 130022, China

electrolyte or hole-transport material.[1] Assembled in a lab from solutions of inexpensive chemicals, device efficiencies of more than 12% have been reported.[2] DSCs hence are a very promising candidate to contribute towards a balanced future energy solution.

High performance DSCs rely upon an extremely high interfacial area, since charge carriers are only generated in the chemisorbed monolayer of photoactive dye. Since O'Regan's and Grätzel's ground breaking work in 1991,[3] this is usually realized by the sintering of TiO_2 nanoparticles into a random network, which delivers over a thousand-fold increase in surface area in a ten micron thick film, as compared to a flat film. Significant progress has since been achieved, mostly by the development of new sensitizers,[4] light management in the device[5–7] and increasing the long term stability.[8] However, since electron transport is very slow in this photoanode, this long established champion electrode faces serious limitations with the development of solid-state DSCs (ss-DSC) which employ an organic hole-transporter as the redox mediator.[9,10] Research efforts to replace the liquid electrolyte with a molecular or polymeric hole conductor are driven by the aim to increase efficiency by reducing the loss-in-potential[11] and to tackle stability issues caused by corrosion and leakage of the liquid electrolyte.[10] Since charge carrier recombination in ss-DSCs can be up to 2 orders of magnitudes faster than in conventional liquid electrolyte devices,[12,13] the poor electron diffusion in these random networks[14–16] combined with poor infiltration of the solid-state hole transporters limit the titania electrode in ss-DSCs to around 2 µm. This is not thick enough to achieve panchromatic light absorption with the currently available sensitizers.

New electrode architectures have been proposed with the aim to control pore size and crystallinity on the 10 nm length scale to limit the effect of these reported problems. Examples include geometries of standing nanowires,[17] fibrous 1-dimensional networks,[18] a bicontinuous gyroid network[19] and the block-copolymer directed assembly of sol-gel material.[20,21]The latter is particularly promising since it allows control of pore size,[21] crystallinity[22] and electronic properties[23] of the photoanode while being compatible with low cost and large scale production methods.

The driving force for the self-assembly of block copolymers is the incompatibility of the covalently linked blocks of the macromolecule, which gives rise to a microphase separation on the 5-50 nm length scale into an assortment of morphologies with quasi-1D, 2D, or 3D continuity. This formation mechanism can be compatibilized with functional inorganic materials by taking advantage of selective interactions, such as hydrogen bonding, to drive sol nanoparticles into just one of the polymer blocks. After the removal of the organic

host, typically in a high-temperature calcination step, the inorganic material can preserve the morphology derived from co-assembly. The groups of Wiesner and Stucky pioneered this method for structure directing silica,[24,25] which was soon exploited for nanostructure control in TiO_2 and other metal oxides.[26–28] In principle, following this route should enable the design of ideal photoanodes with control over both morphology and feature size provided by the block copolymer. Indeed, block copolymer derived TiO_2 has been shown to lead to enhanced electron mobilities when designed to facilitate high temperature heat treatments.[29,30]

Despite the potential, DSCs incorporating self-assembled networks have still not reached the best efficiencies of nanoparticle based films. A major drawback is associated with the large volume contraction of the block copolymer derived films during processing - evaporation of residual solvent, condensation of the inorganic network and in the later stage calcination of the polymer and crystallization. For films exceeding several hundred nm in thickness, this typically leads to crack formation and delamination.[31] Several concepts have been presented where block copolymer assembled photoanodes compete well with nanoparticle films for active layers below 1 µm,[20,30] but it proves difficult to scale with thickness. We have established a route for the deposition of mesoporous block copolymer derived films beyond 2 µm, which significantly increased their efficiencies to over 4%.[32]

An observed drawback of the experimental approaches used to date is the fact that the TiO_2 is generally assembled in the majority phase. Lateral stresses during volume reduction are therefore sufficient to lead to catastrophic crack formation. A further consideration is that the ratio between organic and inorganic material in the synthesis has a strong influence on the electronic properties of the resulting TiO_2.[23] A mainly organic matrix leads to a strongly enhanced density of sub-bandgap electronic states, correlated to a significantly increased photocurrent in the devices. For both reasons, it would be favorable to lower the TiO_2 content in the hybrid composite. However, when reducing the TiO_2 content in a diblock copolymer assembled film, the metal oxide becomes a non-continuous minority phase surrounded by the polymer. Upon calcination of the oxide and thermal combustion of the copolymer, film integrity is almost entirely lost due to removal of the supporting matrix. We previously worked around this by performing calcination in the bulk, and subsequently incorporating the as prepared material into a paste for film processing.[23] However, the favorable ordered structure of the mesoporous assembly is entirely lost through this process. Clearly a more direct route with a 3D continuous network morphology as-made would be preferable.

Here, we present a new self-assembly platform for the fast and straightforward synthesis of mesoporous TiO_2 films, based on the triblock terpolymer poly(isoprene-*b*-styrene-*b*-ethylene oxide). This polymer system directs the co-assembly of the oxide into a gyroid-like morphology, where the minority phase is a 3D interconnecting strut network composed of TiO_2. A further less-intuitive benefit here is that the large organic fraction induces a high density of sub-bandgap states distributed in a narrow and low enough energy band, which maximizes charge generation in this dye-sensitized system. The material proves extremely effective when combined with the state-of-the-art organic dye C220 in solid-state cells, and we report power conversion efficiencies of over 5%.

2 Results and discussion

We have recently reported on the assembly of several network morphologies, including a 3D continuous alternating (single) gyroid niobia network, which arises from the coassembly of a triblock terpolymer poly(isoprene-*b*-styrene-*b*-ethylene oxide). In this configuration, the inorganic resides in the minority phase. Due to the fact that network phases are 3D continuous and self-supporting, the morphology is able to withstand removal of the polymer.[33] A similar system is used in this work. Figure 1a illustrates the chemical configuration: The triblock terpolymer in this work consists of a PI, PS, and PEO block with volume fractions of 31%, 53% and 16% respectively. The introduced TiO_2 sol (blue particles) are expected to preferentially reside in the hydrophilic PEO block due to attractive intermolecular forces.[34] The incompatibility of its covalently linked building blocks leads the macromolecule and its guest to co-assemble towards its energy minimal morphology.[24,35] For the utilized volume fractions, we expect an ordered cubic network such as a single "alternating" gyroid morphology of PEO and inorganics, surrounded by a PS matrix and a complementary gyroid network of PI, as illustrated in Figure 1b.[33] For experimental realization, a PI-*b*-PS-*b*-PEO polymer (ISO) of $M_n = 53.4$kg/mol was dissolved in anisole. Separately a sol stock solution was prepared by adding titanium isopropoxide to HCl. The stock solution was then diluted and added to the polymer solution to match the aimed phase space. After deposition by doctor blade coating onto prepared FTO substrates, the films were annealed at 30 °C in an enclosed atmosphere for 24-48h, then aged at elevated temperatures for another 3 days before being calcined in air at 500 °C to remove the organic structure directing agent and crystallize the inorganic network. See Methods Section for experimental details. The as-cast films had a homogeneously networked morphology throughout the thickness as shown in Figure 1c. The hybrid films were based of an oxide:polymer mass ratio of 0.33:1.0, as-

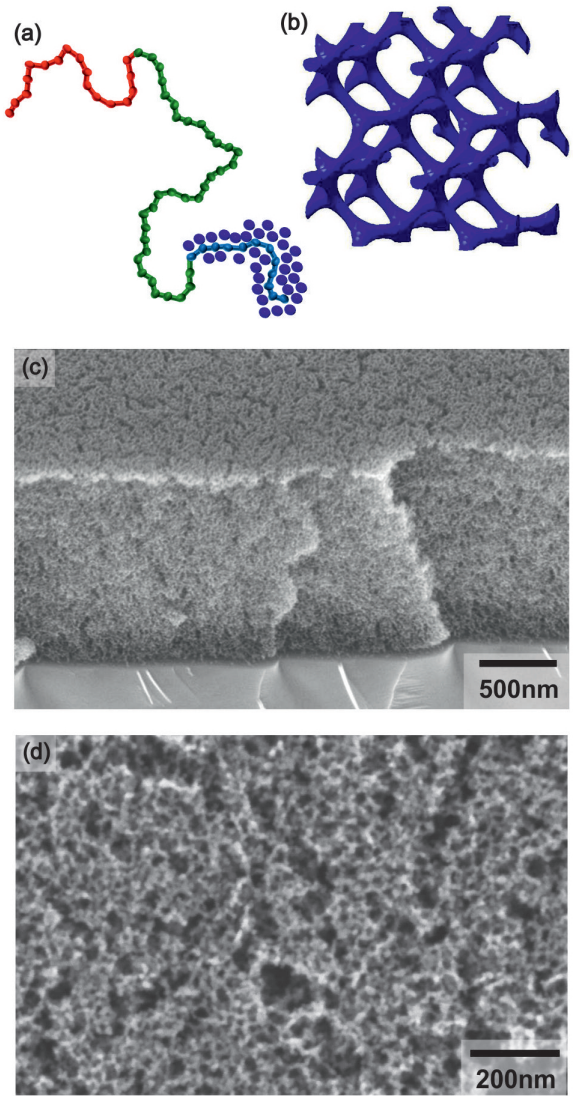

Figure 1. Material system and morphology.(a) The structure-directing macromolecule in this work is a triblock terpolymer poly(isoprene-*b*-styrene-*b*-ethylene oxide) with volume fractions of 31%, 53% and 16% for the isoprene (PI, red), styrene (PS, green) and ethylene oxide block (PEO, blue) respectively. The introduced sol (blue particles) are expected to preferentially reside in the hydrophilic PEO block due to attractive intermolecular forces. Under equilibrium conditions, the incompatibility of its covalently linked building blocks leads the block copolymer and its guest to assemble into its minimal energy morphology, which is in the present configuration an ordered network phase such as the alternating gyroid, where one gyroid network contains the PEO incorporating the oxide sol, and the second gyroid network contains the PI, surrounded by a PS matrix. (b) shows one such gyroid containing the PEO and the oxide phase. (c) Scanning electron microscopy image of a film deposited by doctor blade coating, shown after plasma etching to remove the polymer, which gives rise to a continuous, highly porous TiO_2 network. (d) Close-up scanning electron microscopy image of the mesostructure top surface after calcination at 500 °C exhibiting open and accessible pores.

suming complete condensation to TiO_2. This is equivalent to a volume uptake of 27.5% for the phase of PEO & TiO_2, i.e. the TiO_2 being in the minority phase. The film thickness and overall amount of TiO_2 deposited for each film was controlled with the solution concentration as well as the doctor blading height and velocity. The structural features were preserved throughout the crystallization process resulting in the generation of 20-30 nm mesopores as shown in Figure 1d. In contrast to earlier work using this triblock terpolymer to direct the structure assembly on more equilibrated morphologies in the bulk,[33] we cannot identify a specific space group due to the limited long-range structural ordering for thin film deposition. This is somewhat expected since drying kinetics in thin films lead to a quenching of the microphase separation process by the simultaneous sol-gel reaction before reaching its equilibrium morphology. Nevertheless, the TiO_2 photoanodes exhibit a continuous network of very high porosity which arises from the co-assembly of TiO_2 in the minority phase.

The as-calcined photoanodes were subsequently subject to a $TiCl_4$ treatment and resintering at 500 °C as is conventionally done for dye-sensitized solar cells before being immersed in a dye solution and assembled into a solid-state DSC. Cross-sections of the fully assembled devices are shown in the Supplementary Information. Crystallite sizes are $\sim$ 12 nm for the triblock terpolymer-derived structures and $\sim$ 19 nm for the standard nanoparticle films via Scherrer analysis of the [101] anatase peak (see Supporting Information). The standard method to estimate the surface area and porosity of mesoporous oxides is to perform nitrogen desorption measurements. However, this prooves difficult for thin films and furthermore a measure of the effective accessible surface area for dye adsorption may be more relevant for the electrode material. In order to estimate the surface roughness of the triblock terpolymer derived films we therefore compared the accesible surface area by a dye desorption technique. Firstly, the standard nanoparticle based films, which have been well characterised by nitrogen desorption, were used as a standard control. From nitrogen desorption the standard nanoparticle films have a roughness factor of 116 fold per µm thickness of film. Following overnight sensitization with a ruthenium based dye, termed Z907, and subsequent dye desorption, Uv-Vis absorption measurements of the desorbed dye were taken. The dye was calculated to occupy around 1.6 nm^2 per dye molecule, consistent with reports in literature.[36,37] With the assumption that same dye loading will be achieved on both the anatase titania triblock terpolymer derived films and the standard anatase nanoparticles based films, we calculate the surface roughness to be 161 fold per µm thickness of film for the triblock terpolymer-derived films measured via Z907 dye desorption in

Film	Porosity (vol%)	Surface roughness (per µm)	Crystallite Size (nm)	Average pore diameter (nm)
Nanoparticle	48±4	116	19	18
Triblock	61±3	161	12	21

Table 1. Film characteristics. Values shown correspond to films treated with $TiCl_4$ methanol (see Supporting Information).

In order to estimate the porosity of the films we have used spectroscopic ellipseometry to extract the optical constants for each film, and reconstructed an "effective medium" composed of differing volume fractions of air ($n \approx 1$) and anatase TiO_2 ($n = 2.5$) employing the Bruggeman effective medium approximation.[38] The refractive indices of the films were determined to be 1.39 (triblock terpolymer-derived films before $TiCl_4$), 1.52 (triblock terpolymer-derived films after $TiCl_4$), 1.62 (nanoparticles before $TiCl_4$), and 1.73 (nanoparticles after $TiCl_4$) respectively. It is already apparent simply from these values that the porosity reduces slightly after $TiCl_4$ treatment and that the porosity of the triblock terpolymer films is higher than the nanoparticle films. Specifically, we calculate the porosity of the triblock terpolymer-derived films to be 69±2 vol% before $TiCl_4$ treatment and 61±3 vol% after this surface treatment. In comparison, standard nanoparticle films before $TiCl_4$ treatment are calculated to be 55±2 vol% porous and 48±4 vol% after the surface treatment. The increase in refractive index after the $TiCl_4$ surface treatment corresponds to a $\sim$ 1 nm thick coating of the pore structure for both triblock terpolymer-derived films (average pore diameter $\sim$ 21 nm) and nanoparticle films (average pore diameter $\sim$ 18 nm), respectively. See ref.[39] for details. These porosity and surface area estimations indicate that structurally, the triblock terpolymer exhibits a higher accessible surface are for dye loading as well as enhanced porosity compared to the standard nanoparticle based films. A summary of all film characteristics can be found in Table 1.

Device characterization, shown in Figure 2 reveals the high efficiency of the presented photoanode. For comparison, we have included the device performance of solid-state DSCs assembled from a diblock copolymer directed photoanode, which we have previously presented in a separate publication.[32] Solar cells fabricated from the triblock terpolymer, where the cast hybrid mixture has a majority component of organic material (around 70% by volume), show a comparatively high short-circuit current (J_{sc}) of 6.7 $mAcm^{-2}$, and an open circuit voltage (V_{oc}) of 0.78 V. In the case of a diblock copolymer directed assembly, the TiO_2 resides in the majority phase, with a much higher inorganic to organic volume ratio after film deposition. These photoanodes show an increased V_{oc} of 0.83 V while J_{sc}

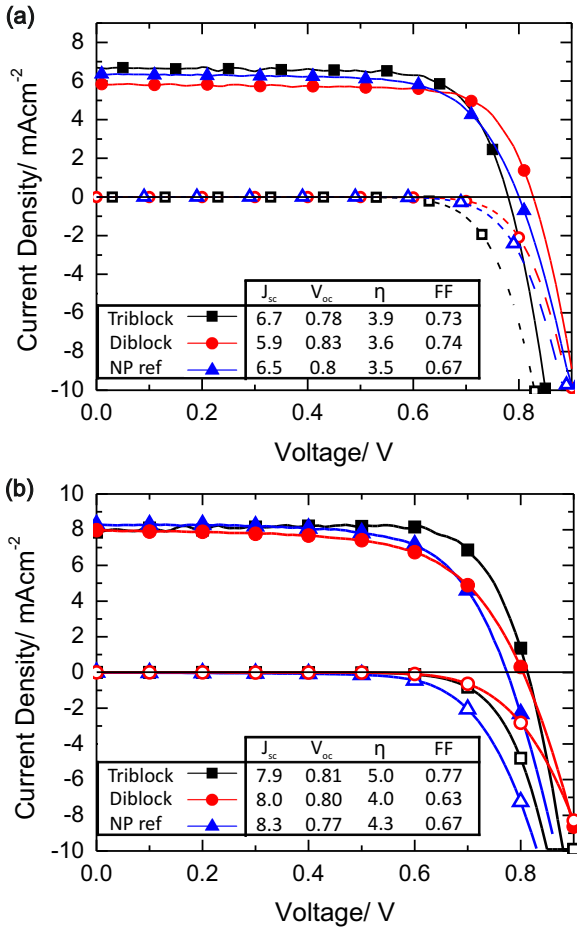

Figure 2. Current-voltage characteristics (a) Current-Voltage curves measured under AM1.5 simulated sun light of 100 mWcm^2 for devices incorporating triblock terpolymer co-assembled networks (black, squares), diblock copolymer co-assembled networks (blue, triangles) and standard nanoparticle based devices (red, circles) employing D102 as the sensitizer. Inset shows solar cell performance parameters for all 3 devices. (b) Current-Voltage curves for solid-state DSCs employing C220 as the dye-sensitizer.[40]

is reduced to 5.8 mAcm^{-2}. Devices based on conventional nanoparticle photoanodes lie in between, with $V_{oc} = 0.80$ V and $J_{sc} = 6.5$ mAcm^{-2}.

These findings are consistent with previous observations of the role of the inorganic to organic ratio in the block copolymer assembly process upon the device properties of the photoanode.[23] The hybrid network within which the TiO_2 resides in during the calcination plays a decisive role for the electronic properties of the mesoporous TiO_2 even after the calcination step and $TiCl_4$ treatment. We have associated this to the reducing characteristic of the organics during polymer oxidation and TiO_2 crystallization at high temperatures. We speculate that the organic materials act as an oxygen sink, favoring the formation of oxygen vacancies which generate sub-bandgap states,[41–44] broadening the tail of the conduction band states and subsequently aiding electron transfer from the photoexcited dye. A mainly organic matrix in the film preparation leads to a significantly increased generation of photocurrent, accompanied by a slight drop in V_{oc} in the final devices. Though photoan-

odes made from triblock terpolymer (highly porous continuous network), diblock copolymer (micellar arrangement) and conventional TiO_2 nanoparticles (random dense packing) are all very different, a similar strong dependence on its "organic to inorganic history" during materials assembly appears to be observed.

For devices incorporating one of the best performing dyes for solid-state DSCs, a donor-pi-acceptor organic dye termed C220,[40] we obtain a striking power conversion efficiency of 5.03% for triblock terpolymer directed photoanodes, shown in Figure 2b. This represents a 16% improvement in performance over standard optimized nanoparticle devices of 1.8 µm in thickness as prepared in our laboratory, demonstrating the potential of this approach for future high efficiency devices. As somewhat of a milestone for this materials approach, on a like-to-like comparison this is the first time the self-assembled oxides have out-performed the conventional state-of-the art nanoparticle based photoanodes in dye-sensitized solar cells. We note that the maximum current from the JV curve for the triblock devices does not occur at short-circuit. This effect is sometimes observed, though not fully understood, for some sensitizers when used in solid-state dye-sensitized solar cells,[45] however investigating its exact nature is outside of the scope of this work.

In our previous work on paste processed TiO_2, we eliminated the effect of the film morphology and found no significant differences in charge transport and recombination.[23] In contrast, here we observe over two-fold increase in charge transport rate at short-circuit for films with diblock copolymer directed structures compared to the ones assembled with the triblock terpolymer (background bias light around 100 $mWcm^{-2}$, see Methods Section for details). This trend is maintained over a wide span of light intensities down to 2 $mWcm^{-2}$, which corresponds to a photocurrent of about 0.2 $mAcm^{-2}$ in these devices. This significant difference, shown in Figure 3a, probably arises from the larger crystal size and the denser TiO_2 network of the diblock copolymer directed structures.[22,46] Recombination dynamics are very similar in all 3 systems, as shown in Figure 3b, where almost all data points overlap at similar background bias light intensities.

Along with higher electron transport rates, we would expect increased photocurrents from systems with better charge collection efficiencies. In contrast, we see a 15% loss in photocurrent for the "highly diffusive" diblock directed films compared to the triblock systems. However, the charge collection efficiency, as calculated from the balance of rates for charge collection and recombination under short-circuit conditions, is over 90% for all systems. To resolve this peculiarity, we have performed differential capacitance-voltage measurements which directly gives us the shape of the sub-bandgap density of states (DOS)

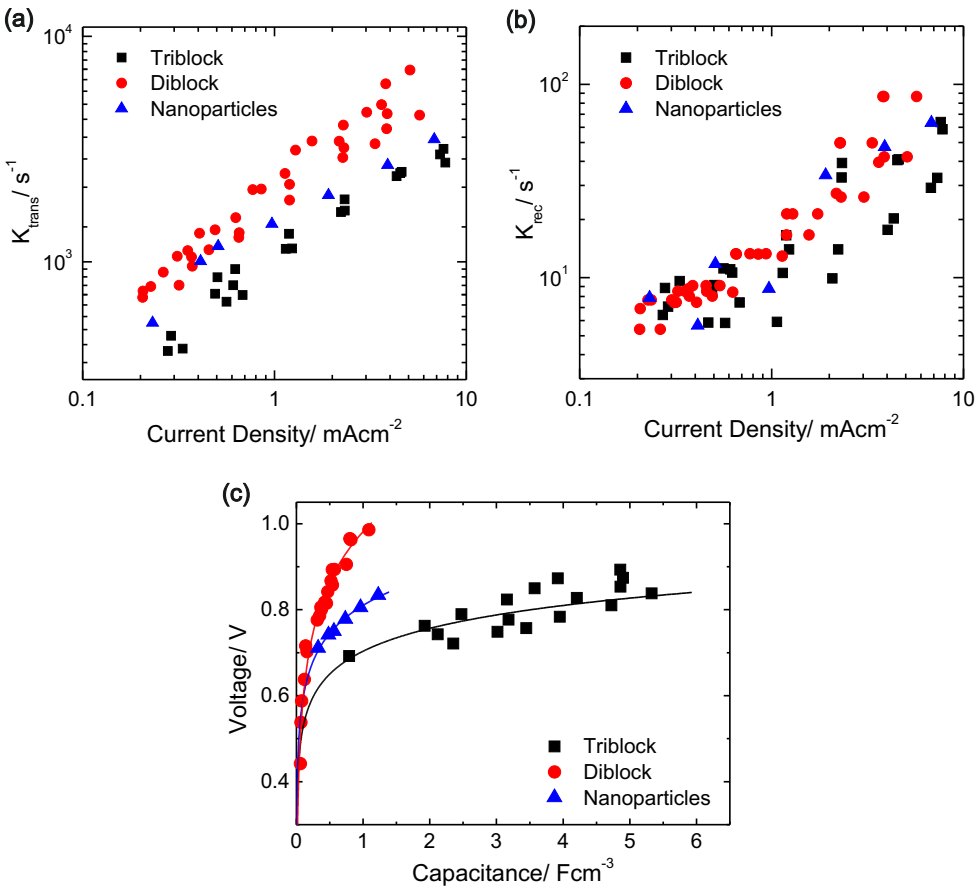

Figure 3. Device characteristics. Transport (a) and recombination (b) rates at short circuit conditions for devices incorporating triblock terpolymer co-assembled networks (black, squares), diblock copolymer co-assembled networks (blue, triangles) and standard nanoparticle based devices (red, circles). (c) Density of states plot per cm^{-3} of titania, for devices incorporating triblock terpolymer co-assembled networks (black, squares), diblock copolymer co-assembled networks (red, circles) and standard nanoparticle based devices (blue, triangles). Lines correspond to single exponential fits of the data points. We note that the transient photocurrent and photovoltage measurements were carried out at short-circuit under potentiostatic or galvanostatic modes respectively, with the short-circuit current set and varied by changing the white light bias.

in the TiO_2 photoanodes. Figure 3c clearly shows a large increase in the sub-bandgap DOS for the triblock devices compared to the diblock solar cells. This effect is consistent with our postulation that the organic components partially reduce the surface of the TiO_2 during thermal degradation and calcination, with the more numerous oxygen vacancies increasing the density of sub-bandgap states. Indeed, others have reported that oxygen vacancies induce adjacent Ti^{4+} ions which generate states $\sim$1 eV below the CB.[43] This suggests that the differences in photovoltaic parameters found in the JV curves of Figure 2 are dominated by the underlying shift in the distribution of sub-bandgap states, rather than charge collection efficiencies, consistent with our previous work.[23] In this instance, not only must the available sub-bandgap states lie at a low enough energy to enable efficient electron transfer, but we must also minimize the energy loss to avoid a trade-off between current

and voltage and hence marginalize performance improvements. In the case of the triblock terpolymer derived structures, the sub-bandgap states are also confined in a relatively narrow energy band, allowing us to maximize the photocurrent while still maintaining minimal losses to open-circuit voltage. This results in higher power conversion efficiencies than standard nanoparticle-based devices measured under similar conditions.

Since the transport rates are around two orders of magnitude faster than recombination rates at short-circuit for all systems studied, we associate the improved functioning of our triblock terpolymer assembled photoanodes to the fact that we can engineer the metal oxide/dye/hole-transporter interface to maximize the availability of sub-bandgap states for electron-transfer, while still maintaining a low enough recombination rate and high enough open-circuit voltage.

3 Conclusions

We have presented a new self-assembly platform for the fast and straightforward synthesis of mesoporous TiO_2 films, based on the triblock terpolymer poly(isoprene-*b*-styrene-*b*-ethylene oxide). Our material route has strong advantages over the state-of-the-art photoanodes in solid-state dye-sensitized solar cells. From a purely materials basis, the terpolymer route enables the direct assembly of a continuous network of anatase TiO_2 resulting in films with extremely high porosity and internal surface area. This assembled material is superior to the standard nanoparticle based films on both dye-loading capacity (for a given thickness) and on open pore area. Electronically, the triblock terpolymer derived TiO_2 exhibits a larger density of sub-bandgap states, than the standard nanoparticle based material. This high availability of sub-bandgap states improves photoinduced electron transfer from the dye-sensitizers. As a consequence, for the first time the self-assembled mesoporous oxide system outperforms the conventional nanoparticle based electrodes fabricated and tested under the same conditions, with power conversion efficiencies of 5% demonstrated. We believe that further optimization in line with this work will most likely arise from decoupling the crystal size of the film with its morphology. Indeed, if bigger crystal sizes could be achieved without comprimising the large availability of sub-bandgap states, surface area or porosity of the films, faster transport and slower recombination can be expected, thus improving the charge collection length and hence the efficiency at working conditions.

4 Experimental

Substrate preparation Fluorine doped tin oxide (FTO) coated glass sheets ($15\,\Omega\Box^{-1}$, Pilkington) were etched with zinc powder and HCl (2 M) to obtain the required electrode pattern. The sheets were then washed with soap (2% Hellmanex in water), deionized water, acetone, methanol and finally treated under an oxygen plasma for 10 minutes to remove any traces of organic residues. The FTO sheets were subsequently coated with a compact layer of TiO_2 (100 nm) by aerosol spray pyrolysis deposition at 450 °C, using air as the carrier gas.

Electrode fabrication

Conventional nanoparticle film

A commercial anatase nanoparticle paste used (Dyesol 18NR-T) was diluted with ethanol at a ratio of 3 ml ethanol per 1 g of paste to obtain final film thicknesses of 1.8 ± 0.1 µm when deposited by doctor blade coating. The resulting films were subsequently calcined at 500 °C (ramped over 1.5 hours) for 30 minutes in air.

Triblock terpolymer derived film

A polymer solution was prepared by dissolving 50 mg of ISO (M_n=14.63, 29.04, and 9.77 kg/mol for I, S, and O, respectively, with a polydispersity of 1.05) in 0.61 mL of anhydrous anisole for at least 1h. In a separate vial a dilute sol stock solution was prepared by quickly adding 5 mL of titanium isopropoxide to 1.6 mL of concentrated 37 wt% HCl(aq) under rapid stirring. Caution must be taken since this addition is violently exothermic and can cause splashing. The closed vial containing the dilute sol stock solution was stirred for 5 min followed by the addition of 10 mL of dry tetrahydrofuran and two additional minutes of stirring. Next, 0.22 mL of the dilute sol stock solution was added to the polymer solution followed by 30 minutes of shaking. The quantity of titania sol added was chosen to correspond to c.a. 27.5 vol% for the combined PEO and titania volume in order to target the network morphology window.[47,48] Films were prepared by doctor blading the final solution onto an FTO substrate with a preformed titania compact layer deposited via spray-pyrolysis. The wet films were allowed to dry on hotplates set to 30 °C for 1-2 days. The dry films were aged at 100 °C for 3 days to further the condensation reaction and then were calcined at 500 °C with a 1 °C/min heating ramp followed by a 1 h hold and natural furnace cooling.

Diblock copolymer derived film

TiO_2 electrodes were fabricated as follows: 0.4 g of a poly(isoprene-*b*-ethylene oxide) block-copolymer (PI-*b*-PEO) (molecular weight $M_n = 34.4$ kg/mol, 28 wt% PEO) was dissolved in 8 ml of an azeotrope solvent mixture of toluene (72.84 w%) and 1-butanol (27.16 w%). A titanium-containing sol was prepared separately by the addition of 1.54 ml titanium(IV) isopropoxide (Sigma Aldrich, 99.999% trace metals basis) to 0.49 ml hydrochloric acid (37%) under vigorous stirring. 5 min after addition of the titania precursor, the sol was added to the polymer solution and subsequently stirred for a further 30 min. Hybrid were then deposited from solution via spin coating (1800 rpm, 20 s) or doctor blading onto the prepared FTO substrates. Subsequently the films were exposed to an annealing protocol on a calibrated hotplate (2000 W with programme regulator, Harry Gestigkeit GmbH), typically for 10 min at 50 °C, followed by a 45 min linear heating ramp to 300 °C and a final dwell time of 5 min at this temperature. The procedure of film deposition and subsequent annealing was repeated several times (typically 3-7 cycles) to match the required film thickness. Finally the stack was calcined at 600 °C (3 hours, heat ramp 5 °C/min, Cole Parmer, EW-33855-35) to remove the organic material, crystallize the TiO_2

Materials characterization

Scanning electron microscopy was carried out on a LEO 1550 FESEM (Zeiss) with a field emission source of 5 kV acceleration voltage. Ellipsometric data were taken on a Nanofilm ep3se imaging ellipsometer and the instrument software was used to analyze the data. Results by imaging ellipsometry were verified with a spectroscopic ellipsometer (Woollam alpha-SE). Wide-angle XRD was performed on calcined films deposited on the FTO coated glass as per device assembly. The measurements were made using a PANalytical MPD Pro using monochromatic $CuK_{\alpha 1}$ radiation, using an X'Celerator linear detector.

Solid-state dye-sensitized solar cell fabrication

The mesoporous electrodes were cut down to size and soaked in a 20 mM $TiCl_4$ aqueous bath for 1 hour at 70 °C in an incubator. After rinsing with deionized water and drying in air, the films were heat treated another time at 500 °C for 45 min in air, then cooled down to 70 °C and finally immersed in a dye solution for 1 hour. The indolene dye used was D102, 0.2 mM in a 1:1 volume ratio of tert-butanol and acetonitrile. Spiro-OMeTAD was dissolved

in chlorobenzene at varying concentrations ranging from 6 vol% to 10 vol%. After fully dissolving the hole transporter, 4-tert-butyl pyridine (tBP) was added with a volume to mass ratio of 1:26 µl/mg tBP:spiro-OMeTAD. Lithium bis(trifluoromethylsulfonyl)imide salt (Li-TFSI) was pre-dissolved in acetonitrile at 170 mg/ml, then added to the hole transporter solution at 1:12 µl/mg of Li-TFSI solution:Spiro-OMeTAD. When changing the hole transporter concentration, these two ratios were kept constant. The dyed films were rinsed briefly in acetonitrile and dried in air for 1 minute. Then a small quantity of the hole transporter solution 18-25 µl was dispensed onto each substrate and left to wet the films for 15 s before spin-coating at 700 rpm for 45 s in air. The films were left for a minimum period of twenty-four hours in air before placing them in a thermal evaporator where 150 nm thick silver electrodes were deposited through a shadow mask under high vacuum (10^{-6} mbar).

Solar cell characterization

Simulated AM 1.5 sunlight was generated with an ABET technologies sun2000 Class A solar simulator calibrated to give 100 mWcm^{-2} using an NREL calibrated KG5 filtered silicon reference cell. The spectral mismatch factor was calculated to be less than 1%. The JV curves were recorded with a Keithley 2400. The Solar Cells were masked with a metal aperture defining the active area of the solar cells and the device holder and measuring apparatus is set up such that no light can enter the sides of the glass substrates. The photovoltage and photocurrent decay measurement[49,50] were performed as described elsewhere.[23,51]

Acknowledgments

This publication is based on work supported in part by Award No. KUS-C1-018-02, made by King Abdullah University of Science and Technology (KAUST), the European Community's Seventh Framework Programme (FP7/2007-2013) under grant agreement n °246124 of the SANS project, the EPSRC (EP/F056702/1 and EP/F065884/1), the Department of Energy (DE-FG02 87ER45298) through the Cornell Fuel Cell Institute (CFCI) and the National Science Foundation (DMR-0605856). M.S. was supported by the Cornell Fuel Cell Institute and the Energy Materials Center at Cornell (EMC2), an Energy Frontier Research Center funded by the U.S. Department of Energy, Office of Science, Office of Basic Energy Sciences under Award Number DE-SC0001086. N.C. and P.W. acknowledge the the National 973

Program (No. 2011CBA00702) for financial support.

[1] A. Hagfeldt, G. Boschloo, L. Sun, L. Kloo, H. Pettersson, *Chem. Rev.* **2010**, *110*, 6595–6663.

[2] A. Yella, H.-W. Lee, H. N. Tsao, C. Yi, A. K. Chandiran, M. Nazeeruddin, E. W.-G. Diau, C.-Y. Yeh, S. M. Zakeeruddin, M. Grtzel, *Science* **2011**, *334*(6056), 629–634.

[3] O'Reagan, Brian and Grätzel, Michael, *Nature* **1991**, *353*, 737–740.

[4] J.-H. Yum, E. Baranoff, S. Wenger, M. K. Nazeeruddin, M. Grätzel, *Energy Environ. Sci.* **2011**, *4*(3), 842.

[5] A. Usami, *Chem. Phys. Lett.* **1997**, *277*, 105–108.

[6] S. Hore, C. Vetter, R. Kern, H. Smit, A. Hinsch, *Sol. Energ. Mat. Sol. C.* **2006**, *90*(9), 1176–1188.

[7] I. G. Yu, Y. J. Kim, H. J. Kim, C. Lee, W. I. Lee, *J. Mater. Chem.* **2010**, , 532–538.

[8] J. M. Kroon, N. J. Bakker, H. J. P. Smit, P. Liska, K. R. Thampi, P. Wang, S. M. Zakeeruddin, M. Grätzel, A. Hinsch, S. Hore, U. Wurfel, R. Sastrawan, J. R. Durrant, E. Palomares, H. Pettersson, T. Gruszecki, J. Walter, K. Skupien, G. E. Tulloch, *Prog. Photovoltaics* **2007**, *15*(1), 1–18.

[9] U. Bach, P. Comte, J. E. Moser, F. Weisso, M. Grätzel, *Nature* **1998**, *395*, 583–585.

[10] H. Snaith, L. Schmidt-Mende, *Adv. Mater.* **2007**, *19*(20), 3187–3200.

[11] H. J. Snaith, *Adv. Funct. Mater.* **2010**, *20*(1), 13–19.

[12] J. Krüger, R. Plass, M. Grätzel, P. Cameron, L. Peter, *J. Phys. Chem. B* **2003**, *107*(31), 7536–7539.

[13] F. Fabregat-Santiago, J. Bisquert, L. Cevey, P. Chen, M. Wang, S. M. Zakeeruddin, M. Grätzel, *J. Am. Chem. Soc.* **2009**, *131*(2), 558–562.

[14] T. Dittrich, E. Lebedev, J. Weidmann, *Phys. Status Solidi A* **1998**, *1998*(165), R5–R6.

[15] H. J. Snaith, M. Grätzel, *Adv. Mater.* **2007**, *19*, 3643–3647.

[16] P. Tiwana, P. Parkinson, M. B. Johnston, H. J. Snaith, L. M. Herz, *J. Phys. Chem. C* **2010**, *114*(2), 1365–1371.

[17] M. Law, L. E. Greene, J. C. Johnson, R. Saykally, P. Yang, *Nature Mater.* **2005**, *4*(6), 455–9.

[18] N. Tétreault, E. Horvath, T. Moehl, J. Brillet, R. Smajda, S. Bungener, N. Cai, P. Wang, S. M. Zakeeruddin, L. Forro, M. Grätzel, *ACS Nano* **2010**, *4*(12), 7644–7650.

[19] E. J. W. Crossland, M. Kamperman, M. Nedelcu, C. Ducati, U. Wiesner, D.-M. Smilgies, G. E. S. Toombes, M. A. Hillmyer, S. Ludwigs, U. Steiner, H. J. Snaith, *Nano Lett.* **2009**, *9*(8), 2807–12.

[20] M. Zukalová, A. Zukal, L. Kavan, M. K. Nazeeruddin, P. Liska, M. Grätzel, *Nano Lett.* **2005**, *5*(9), 1789–92.

[21] M. Nedelcu, J. Lee, E. J. W. Crossland, S. C. Warren, M. C. Orilall, S. Guldin, S. Hüttner, C. Ducati, D. Eder, U. Wiesner, U. Steiner, H. J. Snaith, *Soft Matter* **2009**, *5*(1), 134.

[22] S. Guldin, S. Hüttner, P. Tiwana, M. C. Orilall, B. Ülgüt, M. Stefik, P. Docampo, M. Kolle, G. Divitini, C. Ducati, S. A. T. Redfern, H. J. Snaith, U. Wiesner, D. Eder, U. Steiner, *Energy Environ. Sci.* **2011**, *4*(1), 225–233.

[23] P. Docampo, S. Guldin, M. Stefik, P. Tiwana, M. C. Orilall, S. Hüttner, H. Sai, U. Wiesner, U. Steiner, H. J. Snaith, *Adv. Funct. Mater.* **2010**, *20*(11), 1787 – 1796.

[24] M. Templin, A. Franck, A. DuChesne, H. Leist, Y. Zhang, R. Ulrich, V. Schädler, U. Wiesner, *Science* **1997**, *278*(5344), 1795–1798.

[25] D. Zhao, J. Feng, Q. Huo, N. Melosh, G. Fredrickson, B. Chmelka, G. Stucky, *Science* **1998**, *279*(5350), 548–552.

[26] P. Yang, D. Zhao, D. Margolese, B. Chmelka, G. Stucky, *Nature* **1998**, *396*(6707), 152–155.

[27] E. Crepaldi, G. Soler-Illia, D. Grosso, F. Cagnol, F. Ribot, C. Sanchez, *J. Am. Chem. Soc.* **2003**, *125*(32), 9770–9786.

[28] B. Smarsly, D. Grosso, T. Brezesinski, N. Pinna, C. Boissiere, M. Antonietti, C. Sanchez, *Chem. Mater.* **2004**, *16*(15), 2948–2952.

[29] J. Lee, M. C. Orilall, S. C. Warren, M. Kamperman, F. J. DiSalvo, U. Wiesner, *Nature Mater.* **2008**, *7*(3), 222–8.

[30] S. Guldin, S. Hüttner, P. Tiwana, M. C. Orilall, B. Ülgüt, M. Stefik, P. Docampo, M. Kolle, G. Divitini, C. Ducati, S. A. T. Redfern, H. J. Snaith, U. Wiesner, D. Eder, U. Steiner, *Energy Environ. Sci.* **2011**, *4*(1), 225–233.

[31] S. Choi, M. Mamak, N. Coombs, N. Chopra, G. A. Ozin, *Adv. Funct. Mater.* **2004**, *14*(4), 335–344.

[32] S. Guldin, P. Docampo, M. Stefik, G. Kamita, U. Wiesner, H. J. Snaith, U. Steiner, *Small* **2011**, , DOI: 10.1002/smll.201102063.

[33] M. Stefik, S. Wang, R. Hovden, H. Sai, M. W. Tate, D. A. Muller, U. Steiner, S. M. Gruner, U. Wiesner, *J. Mater. Chem.* **2012**, *22*(3), 1078–1087.

[34] S. Bagshaw, E. Prouzet, T. Pinnavaia, *Science* **1995**, *269*(5228), 1242–1244.

[35] P. Simon, R. Ulrich, H. Spiess, U. Wiesner, *Chem. Mater.* **2001**, *13*(10), 3464–3486.

[36] V. Shklover, Y. E. Ovchinnikov, L. S. Braginsky, S. M. Zakeeruddin, M. Grätzel, *Chem. Mater.* **1998**, *10*(9), 2533–2541.

[37] G. Bazzan, J. R. Deneault, T.-S. Kang, B. E. Taylor, M. F. Durstock, *Adv. Funct. Mater.* **2011**, *21*(17), 3268–3274.

[38] D. A. G. Bruggeman, *Ann. Phys.* **1935**, *24*(7), 636–664.

[39] S. Guldin, M. Kolle, M. Stefik, R. Langford, D. Eder, U. Wiesner, U. Steiner, *Adv. Mater.* **2011**, *23*(32), 3664–3668.

[40] N. Cai, S.-J. Moon, L. Cevey-Ha, T. Moehl, R. Humphry-Baker, P. Wang, S. M. Zakeeruddin, M. Grätzel, *Nano Lett.* **2011**, *11*(4), 1452–1456.

[41] B. J. Morgan, G. W. Watson, *Surf. Sci.* **2007**, *601*(21), 5034 – 5041.

[42] V. E. Henrich, G. Dresselhaus, H. J. Zeiger, *Phys. Rev. Lett.* **1976**, *36*, 1335–1339.

[43] P. Kumar, S. Badrinarayanan, M. Sastry, *Thin Solid Films* **2000**, *358*(1-2), 122 – 130.

[44] W.-T. Kim, C.-D. Kim, Q. W. Choi, *Phys. Rev. B* **1984**, *30*, 3625–3628.

[45] H. J. Snaith, A. Petrozza, S. Ito, H. Miura, M. Grtzel, *Advanced Functional Materials* **2009**, *19*(11), 1810–1818.

[46] K. D. Benkstein, N. Kopidakis, J. van de Lagemaat, A. J. Frank, *J. Phys. Chem. B* **2003**, *107*(31), 7759–7767.

[47] M. Stefik, S. Mahajan, H. Sai, T. H. Epps, F. S. Bates, S. M. Gruner, F. J. DiSalvo, U. Wiesner, *Chem. Mater.* **2009**, *21*(22), 5466–5473.

[48] C. A. Tyler, J. Qin, F. S. Bates, D. C. Morse, *Macromolecules* **2007**, *40*(13), 4654–4668.

[49] B. O'Regan, F. Lenzmann, *J. Phys. Chem. B* **2004**, *108*(14), 4342–4350.

[50] J. Bisquert, A. Zaban, M. Greenshtein, I. Mora-Sero, *J. Am. Chem. Soc.* **2004**, *126*(41), 13550–13559.

[51] H. J. Snaith, R. Humphry-Baker, P. Chen, I. Cesar, S. M. Zakeeruddin, M. Grätzel, *Nanotechnology 19*(42), .